Am J Transl Res 2021;13(8):9182-9194
www.ajtr.org /ISSN:1943-8141/AJTR0130368

Original Article

T2-FLAIR, DWI and DKI radiomics satisfactorily predicts histological grade and Ki-67 proliferation index in gliomas

Changliang Su[1], Xiaowei Chen[2], Chenxia Liu[2], Shihui Li[2], Jingjing Jiang[2], Yuanyun Qin[2], Shun Zhang[2]

[1]Department of Medical Imaging, Sun Yat-sen University Cancer Center; State Key Laboratory of Oncology in South China; Collaborative Innovation Center for Cancer Medicine, Guangzhou 510060, China; [2]Department of Radiology, Tongji Hospital, Tongji Medical College, Huazhong University of Science and Technology, Wuhan, Hubei, China

Received January 19, 2021; Accepted May 26, 2021; Epub August 15, 2021; Published August 30, 2021

Abstract: Objective: To build highly predictive performance models for glioma stratification with radiomics features from non-invasive MRI. Methods: T2-weighted fluid-attenuated inversion recovery (T2-FLAIR) imaging, diffusion-weighted MRI and diffusion kurtosis imaging were retrospectively collected for 139 glioma cases (2 with grade I, 67 with grade II, 36 with grade III and 34 with grade IV disease). Multi-parameter maps, including the apparent diffusion coefficient (ADC), mean diffusion coefficient (Dmean), fractional anisotropy (FA), and mean kurtosis (MK), were co-registered to T2-FLAIR, and 431 radiomics features for each were extracted within manually segmented tumour regions. Partial correlation analysis revealed correlations between radiomics features and glioma stratification factors (tumour grades and Ki-67 LI). Predictive models were built with adjusted-imbalanced logistic regression. Results: MK radiomics features were more closely correlated with glioma stratification than other modalities analysed. The maximum R in MK was 0.52 for tumour grade and 0.56 for Ki-67 index (compared with 0.36 and 0.34 in FA, and 0.43 and 0.37 in ADC, and 0.48 and 0.42 in T2-FLAIR). The best predictive models for grade II vs. III, grade II vs. IV, low-grade vs. high-grade gliomas and positive vs. highly positive Ki-67 LI were obtained by combining multi-parameter MR radiomics features with AUCs of 0.858, 0.966, 0.853 and 0.870, respectively. However, for grade III vs. IV gliomas, the model obtained from MK radiomics features achieved the highest AUC (0.947), with excellent sensitivity and specificity. Conclusion: Compared with the other modalities, MK showed closer correlations with tumour grade and Ki-67 LI. Combined radiomics models integrating multi-parameter MRI allow for the generation of highly predictive models for glioma stratification.

Keywords: Magnetic resonance imaging, diffusion kurtosis imaging, radiomics, glioma, stratification

Introduction

Glioma is the most common primary brain cancer with high malignancy, and causes great harm to a patient's wellbeing, society, and the economy [1]. Surgical resection plus radio-/chemotherapy following adjuvant chemotherapy has greatly improved patient prognosis [2]. However, the survival prognosis is still not favourable. Although genetic markers play an important role in providing appropriate treatment, the tumour grade and proliferation index are still generally used prognostic biomarkers for glioma stratification, treatment design and prognosis prediction [3, 4]. Different grade gliomas respond differently to treatment regimens, resulting in various survival times [5-7]. The Ki-67 labelling index (Ki-67 LI) correlates with tumour malignancy, and its prognostic value is independent of IDH status [8, 9]. An accurate determination of tumour malignancy and proliferation is vital for designing treatment regimens and adjusting treatment plans, especially for patients who failed isocitrate dehydrogenase (IDH) genotype testing. However, the stratification of glioma grades and proliferation activities mainly relies on post-surgical pathological examination, which is time consuming and suffers from biases related to tissue sample selection or unexpected risks. Consequently,

robust and non-invasive biomarkers for glioma could facilitate clinical management and improve the patient hospitalization experience.

Functional and physiological MRI supplies metabolic and physiological information and reflects tumour pathophysiological stages [10]. Diffusion-weighted MR imaging (DWI) exhibits great superiority to anatomical MRI in imaging-restricted water diffusion in brain diseases [11, 12], and diffusion tensor imaging (DTI) has been used extensively to depict localization in relation to white matter tracts (infiltration, deflection) [13]. Diffusion kurtosis imaging (DKI) estimates the kurtosis of the water diffusion probability distribution function [14]. The metrics of DKI include the mean diffusion coefficient (Dmean), fractional anisotropy (FA), and mean kurtosis (MK). MK is regarded as a quantitative parameter evaluating the non-Gaussian distribution diffusion status, which is strongly linked to the cellular microstructure and provides additional information to resolve intravoxel fibre crossings [15]. Previous studies have demonstrated the feasibility of DKI metrics in glioma grading and proliferation prediction; however, the accuracies still need to be improved, especially for the differentiation of grade II vs. III gliomas and grade III vs. IV gliomas [15, 16].

Radiomics has emerged as a promising tool for the precise management of cancer patients via a large number of features extracted from medical images [17, 18]. Radiomics allows for signal or density changes to be captured in medical images that cannot be observed merely with the naked eye. Integrated by machine learning algorithms, high-dimensional radiomics feature has resulted in highly predictive diagnostic prognostic models, providing valuable tools for precision medicine [19]. Numerous studies have demonstrated the advanced application value of this approach in differentiating tumour stages, improving disease stratification, predicting treatment responses and estimating patient prognosis [20-22]. For gliomas, radiomics models that predict histological grades, molecular features and prognoses have shown acceptable accuracies [23-25]. However, few studies have focused on the application of DKI radiomics in stratifying gliomas.

Unlike T1 post-contrast enhancement (T1C), T2-weighted fluid-attenuated inversion recovery (T2-FLAIR) imaging provides anatomical information without the administration of contrast agents. In this retrospective study, we aimed to explore and compare the different correlation patterns of radiomics features extracted from T2-FLAIR imaging, DWI and DKI with tumour grades and the Ki-67 labeling index (Ki-67 LI) and to build highly accurate non-invasive models using multi-parameter MRI radiomics for glioma stratification.

Materials and methods

After obtaining approval from the institutional ethics committee of the research hospital (ethics approval number: TJ-IRB20190309), this retrospective study was performed in accordance with the tenets outlined in the Declaration of Helsinki. All scans were performed between October 2013 and January 2016 in a single tertiary hospital, and informed consent was waived.

Patients

A total of 146 glioma patients underwent an MRI scan on a 3.0 Tesla scanner (Discovery MR750, GE Healthcare) with a 32-channel head coil. The inclusion criteria were as follows: (1) histopathological examination confirmed glioma; and (2) intact T2-FLAIR imaging, DWI and DKI data. Six patients were excluded due to a lack of T2-FLAIR imaging and/or DWI data, and one was excluded due to incomplete DKI data. Ultimately, 139 patients with gliomas confirmed by histopathological examination were included, among whom two had grade I, 67 had grade II, 36 had grade III, and 34 had grade IV gliomas according to the 2016 WHO Classification of Tumours of the Central Nervous System [26]. A total of 132 specimens were also subjected to immunohistopathological staining to quantify the Ki-67 LI, in which a Ki-67 LI ≥15% was regarded as highly positive staining and a Ki-67 LI <15% was regarded as positive staining, considering the impact of Ki-67 LI on patient survival [27]. No significant differences in sex were observed among patients with grade II, III and IV gliomas (Table S1), and no significant differences in subtype were observed, except for grade II vs. IV gliomas (39.01±14.10 vs. 49.59±13.56, P =

0.001, Table S1). The study flowchart is summarized in **Figure 1**.

Data acquisition

The MRI protocol included routine MRI, DWI and DKI, and scanning parameters are concisely summarized in Table S2. The routine MRI sequences included T2-weighted fast spin echo imaging (T2FSE), T1C, and T2-FLAIR, and all sequences covered the whole brain, with 20 slices. A two-dimensional DWI sequence with three diffusion directions was implemented with two b values (0 and 1,000 s/mm^2), and the DWI orientation was automatically copied from the routine MRI protocol. For DKI, the EPI-DWI sequence was implemented with two different b values (1,250 and 2,500 s/mm^2) at 25 encoding diffusion directions, and two non-diffusion-weighted images (b = 0 s/mm^2) were acquired. The total scanning duration was 5 minutes and 45 seconds.

Data pre-processing

All routine MR images were co-registered to T2-FLAIR images in SPM (Wellcome Department of Imaging Neuroscience, London, UK; (http://www.fil.ion.ucl.ac.uk/spm/software/spm8/), and the diffusion-related parameters were co-registered to T2-FLAIR images via a B0 map. After co-registration, all images were re-sliced to isotropic 1 mm^3 for radiomics feature extraction.

The scanned diffusional images were implemented with eddy current correction and realignment in FSL (The Oxford Centre for Functional MRI of the Brain, London, UK (https://fsl.fmrib.ox.ac.uk/fsl/fslwiki/). After skull stripping, parameters from DWI and DKI images were calculated. The apparent diffusion coefficient (ADC) was obtained with the following equation: ADC = -ln (SI_{b1000}/SI_{b0})/1000, in which SI_{b1000} and SI_{b0} represent the signal intensities of images with b = 1,000 and 0 s/mm^2, respectively. DKI parameters, i.e., conventional diffusion metrics (Dmean), DTI metrics (FA) and kurtosis metrics (MK), were estimated with a diffusion kurtosis estimator (DKE, https://www.nitrc.org/projects/dke) using the constrained linear least squares-quadratic algorithm after smoothing [28]. To reduce the impact of noise and misregistration, DK images were smoothed using a Gaussian kernel.

Definition of tumour regions

Multi-modal MR images were employed to identify tumour regions, and a semi-automatic method based on the signal intensity threshold in tumour lesions was implemented to depict the tumour area, as introduced by Jiang et al. [15]. Tumour areas were mainly defined as areas with hyperintensity on T2-FLAIR and T1C images with contrast enhancement. With the aid of DWI, necrotic and cystic areas were avoided. The detailed steps and representative tumour regions are displayed in Figure S1. The obtained tumour areas were re-sliced to 1 mm^3 isotropically for radiomics feature extraction.

Radiomics features

Four categories of features as described by Hugo et al. [29] were extracted from T2-FLAIR images, ADC, Dmean, FA and MK maps with in-house software implemented in the MATLAB platform (v13.0, MathWorks, Natick, MA, USA). These features were generally sorted as follows: (1) 14 histogram features; (2) 8 shape-/size-based features; (3) 33 textural features; and (4) 376 wavelet features calculated after the signal wavelet transform with eight bandwidths [(histogram features + texture features) * 8]. Hence, a total of 2,155 features (5 maps * 431 features) were included for each patient.

Statistical analysis

To reveal correlations between radiomics features and tumour grade and the Ki-67 LI, partial correlation analysis was employed in the univariate analysis, in which age and sex were regarded as control variables. Significant *P* values (less than 0.05), FDR-corrected *P* values and Bonferroni-corrected *P* values ($P_{corrected}$ = 1.93E-05) were calculated and compared within different maps. False discovery rate correction was implemented with a linear step-up (LSU) procedure [30]. The differences in age and the Ki-67 LI were tested with one-way ANOVA, and post hoc analysis was performed with the least significant difference method. Differences in sex in glioma patients with different grades were assessed using Fisher's exact test.

An imbalanced-adjusted logistic regression method was utilized to build highly predictive linear regression models in the multivariate

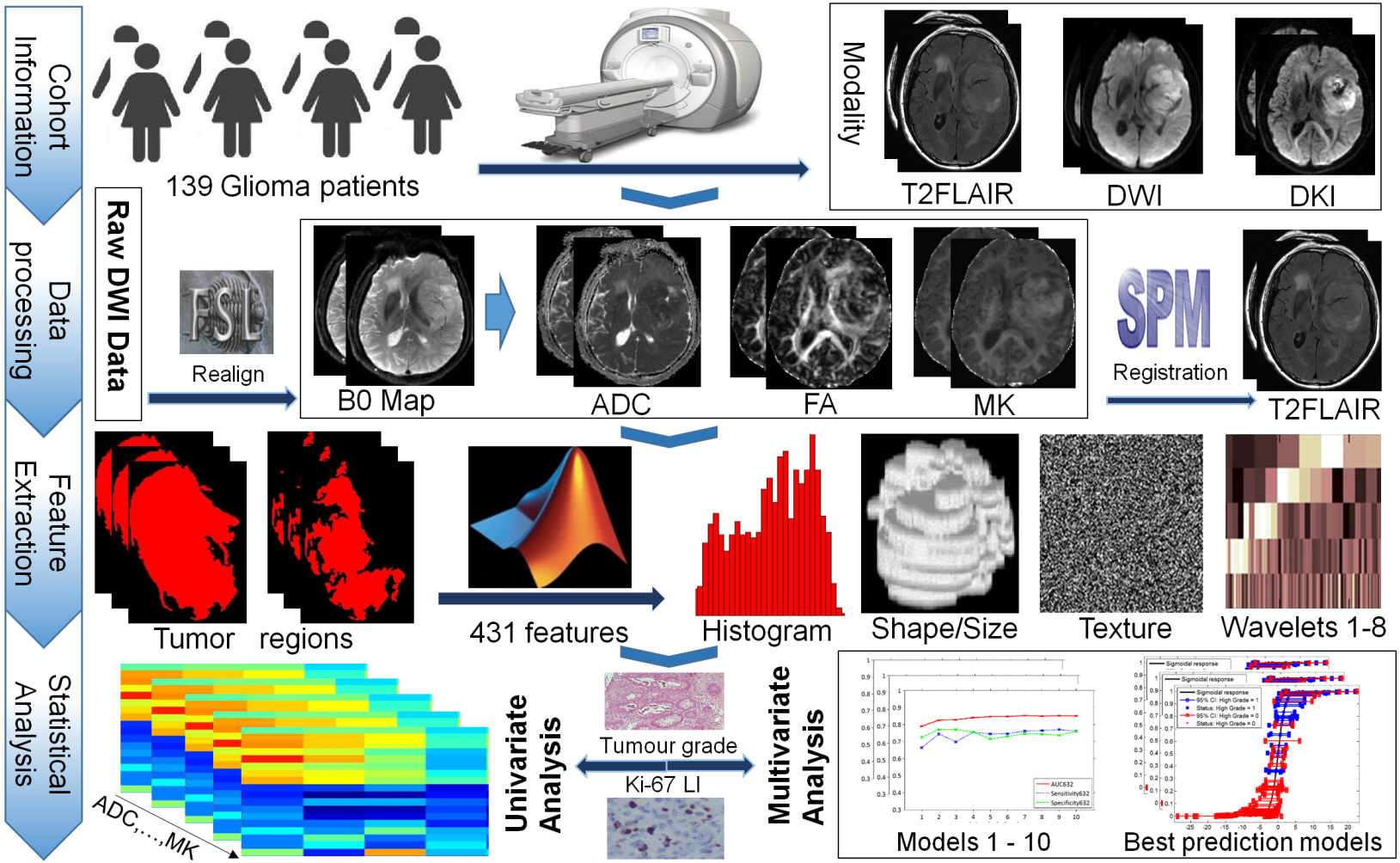

Figure 1. Workflow chart of the radiomics analysis of T2FLAIR, DWI and DKI. I. Data information. A total of 139 patients were included in this comparative study. II. Data pre-processing. Diffusion images were realigned to the B0 map within FSL, and quantitative parameters including ADC, Dmean, FA and MK, were obtained. All images were co-registered to T2-FLAIR within SPM8 and then re-sliced to 1 mm^3 isotropically. III. Feature extraction. A total of 431 features, including histogram features, shape- and size-based features, texture features and wavelet features, were extracted from each map. IV. Statistical analysis. The correlations between radiomics features and pathological characteristics were explored via univariate and multivariate analyses, and the best predictive models were obtained for each subgroup analysis. Five maps, i.e., T2-FLAIR, ADC, Dmean, FA and MK, were obtained.

analysis for the differentiation of glioma subtypes and Ki-67 LI. The multivariate analysis method has been reported by Vallières and colleagues, and a detailed description can be found in the related publication [31] and summarized briefly below. For the combinations of features from each single parameter or all parameters, feature datasets were reduced to 25 features in 1,000 bootstrap samplings, as selected by maximizing the area under the receiver operating characteristic curve $(AUC)_{632+}$ metric [32]. With imbalanced-adjusted logistic regression, the selected features were used to build 1 to 10 models in each subanalysis, and the best predictive models with the highest AUC were selected from models 1-10.

Results

The radiomics features obtained from MK demonstrated closer correlations with the tumour grade and proliferation index than did the other modalities

The *P* value of nearly half of the radiomics features for each contrast was less than 0.05. Moreover, most of the features passed FDR correction, and some withstood strict Bonferroni correction (**Table 1**; **Figure 2**). All the maximum correlation coefficients in each map were above 0.4, except for that in the FA map (0.36, **Table 1**). For the Ki-67 LI, all correlation coefficients were greater than 0.3 (**Table 1**). In the comparison of multi-parameter maps, radiomics features from MK showed the closest correlations with tumour grade and Ki-67 LI.

The numbers of features correlating with tumour grade that had a *P* value less than 0.05, $P_{FDR\ corrected}$ and $P_{Bonferroni\ corrected}$ for MK, were 293, 247 and 56, respectively, which were notably higher than those for T2-FLAIR, ADC, Dmean and FA (**Table 1**). The maximum R of MK features that correlated with tumour grade was 0.52 (compared to 0.48 for T2-FLAIR, 0.43 for ADC, 0.48 for Dmean and 0.36 for FA). For the Ki-67 LI, MK features showed distinct advantages in correlating with tumour biomarkers, and the number of significant radiomics features was greater than that in T2-FLAIR, ADC and FA (**Table 1**). The max R was 0.56 for MK in the Ki-67 LI, 0.42 for T2-FLAIR, 0.37 for ADC, 0.42 for Dmean, and 0.34 for FA. The detailed results are summarized in **Table 1**.

Models built with radiomics features from each map can be used to efficiently stratify gliomas and predict Ki-67 expression levels.

The AUCs of the models built separately with five contrast maps, i.e., T2-FLAIR, ADC, Dmean, FA and MK, ranged from 0.706 to 0.836 for differentiating low-/high-grade gliomas and from 0.75 to 0.865 for predicting positive and highly positive Ki-67 LI. Subsequent analysis revealed that the AUCs varied from 0.715 to 0.791 for differentiating grade II vs. grade III gliomas, 0.882 to 0.947 for differentiating grade II vs. grade IV gliomas and 0.828 to 0.947 for differentiating grade III vs. grade IV gliomas.

For the stratification of glioma subtypes, comparable accuracy was observed between T2-FLAIR, ADC, Dmean, FA and MK for differentiating grade II vs. III gliomas (T2-FLAIR vs. ADC vs. Dmean vs. FA vs. MK: 0.724 vs. 0.745 vs. 0.777 vs. 0.791 vs. 0.715) and for differentiating grade II vs. IV gliomas (T2-FLAIR vs. ADC vs. Dmean vs FA vs. MK: 0.932 vs. 0.911 vs. 0.947 vs. 0.882 vs. 0.916). However, MK radiomics features exhibited outstanding diagnostic performance for differentiating grade III vs. IV gliomas compared with the other maps (T2-FLAIR vs. ADC vs. Dmean vs. FA vs. MK: 0.830 vs. 0.845 vs. 0.828 vs. 0.829 vs. 0.947). This excellent differentiation accuracy implies a distinctive difference in the non-Gaussian diffusion status between grade III and IV gliomas. Moreover, the Dmean extracted from DKI exhibited a diagnostic performance similar to that of ADC. The detailed AUCs, sensitivity and specificity for each map in differentiating glioma subtypes are listed in Tables S3 and S4.

Combining multi-modal MR radiomics features improves the diagnostic performance for glioma stratification, except the differentiation of grade III vs. IV gliomas in MK

The best predictive AUCs for differentiating low-/high-grade gliomas and positive/highly positive Ki-67 LI were obtained with the combination of all multi-parameter MRI radiomics features (AUCs: 0.853 and 0.87 retrospectively, **Figure 3** and Table S3). By combining the features of all contrast maps, similar high differentiation performances were also obtained in

Table 1. Correlations among radiomics features with tumour grade and Ki-67 LI

SeqName	Tumour Grade					Ki-67 LI				
	P<0.05	$P<P_{fdr}$ [a]	$P<P_{corrected}$	Max R	*P* value	P<0.05	$P<P_{fdr}$ [b]	$P<P_{corrected}$	Max R	*P* value
T2-FLAIR	230	152	11	0.48	3.54E-09	199	115	2	0.42	7.5E-06
ADC	203	138	9	0.43	1.42E-07	196	114	0	0.37	1E-04
Dmean	164	92	12	0.48	3.07E-09	167	67	5	0.42	1.18E-05
FA	199	105	1	0.36	1.74E-05	155	63	0	0.34	4.5E-04
MK	293	247	56	0.52	6.52E-11	272	210	25	0.56	7.55E-10

Note: The correlation analysis results of radiomics features with the tumour grade and Ki-67 LI were revealed with partial correlation analysis. Significant *P* values (less than 0.05), FDR-corrected *P* values and Bonferroni-corrected *P* values are listed above. P_{fdr} [a] represents the *P* value threshold at 0.016 for the tumour grades, and P_{fdr} [b] represents the *P* value threshold at 0.013 for the Ki-67 LI.

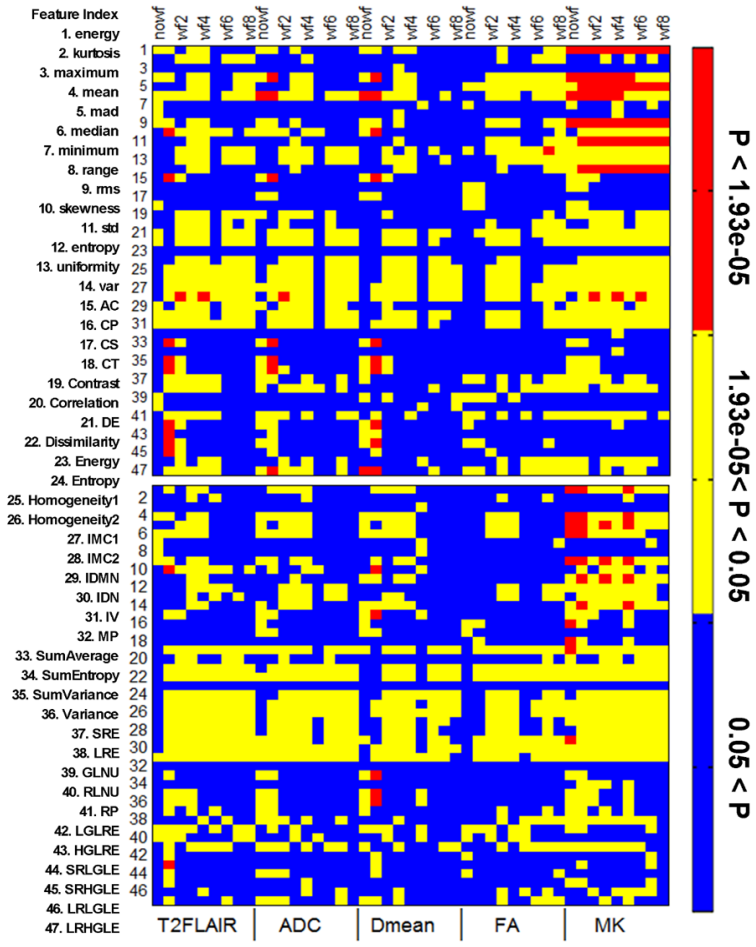

Figure 2. Heat maps of correlation *P* values between non-shape-/size-based features and tumour pathological biomarkers. The X axis on the bottom lists the name of each contrast, and the X axis on the top displays nine catalogues of radiomics features in each contrast. Abbreviations: Nonwf, non-wavelet features; Wf1-8, wavelet features calculated from wavelet bandwidths 1-8. The Y axis (left) shows feature names, and the colour bar of the *P* value range is shown on the right Y axis. Radiomics features from each contrast map correlated with the tumour grade (A) and Ki-67 LI (B) in different patterns, in which MK had the closest correlations with the two pathological biomarkers. For the colour bar, red represents a *P* value less than the Bonferroni corrected *P* value of 1.93E-05, blue represents P>0.05, and yellow represents a *P* value between the two.

differentiating grade II vs. IV gliomas and grade II vs. III gliomas, with AUCs ranging from 0.858 to 0.966 (**Figure 3** and Table S4). For grade III vs. IV gliomas, the best predictive models were obtained from MK radiomics features (AUC: 0.947), and the combination of all multi-parameter MRI radiomics features resulted in an excellent AUC of 0.877. The best diagnostic models for differentiating glioma subtypes are listed in **Table 2**, the corresponding diagnostic performances of the best predictive models are summarized in Tables S3 and S4, and the differentiating effects of the best predictive models are displayed in **Figures 4** and **5**.

Discussion

By conducting a comparative study, we compared the different correlation patterns of radiomics based on T2-FLAIR imaging, DWI and DKI with glioma grade and tumour proliferation. MK radiomics showed closer and stronger correlations with pathological profiles than T2-FLAIR, ADC and FA radiomics. The combination of multi-modal radiomics features from T2-FLAIR imaging, DWI and DKI achieves highly accurate predictive models for

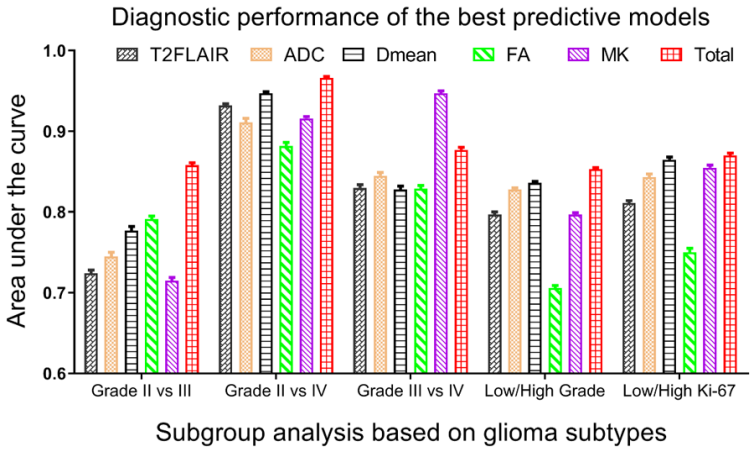

Figure 3. AUCs of the obtained predictive models in each subgroup analysis. The Y axis represents the AUC value, and the X axis value represents the subgroup analysis comparison. The AUCs of the models built with radiomics features from a single map and a combination of all five maps are displayed, and the best predictive performances were obtained when a combination of multi-modal radiomics features was used, except in differentiating grade III and IV gliomas with MK.

glioma stratification; however, the models obtained from MK radiomics achieved the highest diagnostic performance in differentiating grade III and IV gliomas.

The radiomics features from T2-FLAIR imaging, DWI and DKI correlated significantly with tumour grade and Ki-67 LI; however, the radiomics features from MK showed closer correlations than did the other modalities. The more malignant the tumour is, the more heterogeneous the intra-tumour lesion [33]. Radiomics features can be used to extensively measure changes in signals or parameters that occur during oncogenesis in brain cancer [34], which allows for a more accurate quantitative characterization of inter- and intra-tumour heterogeneity. With a three-dimensional volume of interest, radiomics methods contribute to the comprehensive evaluation of parameter changes in the whole tumour volume, which meets increasing demands for a thorough investigation of variations in tumour entities [35].

MK radiomics features significantly correlated with the tumour grade and Ki-67 LI with a profound *P* value, indicating that MK could be a reliable and robust metric for revealing intra-tumour heterogeneity. The subtypes of high-grade gliomas share similar invasive growth patterns, which makes it difficult to distinguish them merely by radiographic methods [1]; however, excellent diagnostic performances in differentiating grade III and IV gliomas were demonstrated in our study, especially for MK. High-grade gliomas have an increased cell density and a rapid growth rate, making their in vivo micro-structures complex; thus, free water diffusion is more likely than non-Gaussian diffusion. Although Gaussian distribution diffusion models such as DWI and DTI have demonstrated priority in stroke and gliomas [36-38], MK can be used to quantify the distinctive non-Gaussian water diffusion observed within glioma subtypes. MK is strongly linked to the cellular microstructure and shows advantages for imaging the brain microstructure [14, 39], making it valuable in differentiating grade III and IV gliomas.

The combination of multi-modal radiomics features can be used to build precise models for predicting the tumour grade and proliferation capability of tumour cells, allowing for the precise stratification of glioma subtypes. Multi-parameter MRI reflects the water content, Gaussian distribution diffusion status, and non-Gaussian diffusion status in tumour lesions [39]. The predictive models obtained in our study for glioma stratification were totally non-invasive and not dependent on contrast-enhanced MRI modalities, which are of vital clinical importance, especially for patients with impaired renal function. A previous meta-analysis demonstrated the priority of MK in identifying low-/high-grade gliomas, which was in accordance with some of our results [16]. Different from one published study in which DKI was employed to differentiate low-grade glioma and glioblastoma [40], we extended the application of DKI radiomics to differentiate glioma subtypes, i.e., predicting grade II, III and IV gliomas and different proliferation levels, and we achieved excellent diagnostic performances with a relatively large patient cohort.

Table 2. Best predictive performance models for each subgroup analysis

Subgroup analysis	β and X	β0
Grade II vs. III	β = [0.8108; 0.05609; -20.46; 0.02874; -3.507E-05; 24.82; -0.8153; -2.053; -0.006119]; X = [Dmean-wf1-Autocorrelation; MK-wf1-median; T2-FLAIR-wf4-LGLRE; Dmean-nonwf-mad; MK-nonwf-energy; FA-wf7-IMC1; Dmean-wf1-Variance; Dmean-wf1-skewness; Dmean-wf1-median]	3.765
Grade II vs. IV	β = [-0.1635; -0.005163; -0.01886; -167.1; 0.003138; -0.03517; -8.046; 0.09591; 0.1291]; X = [T2-FLAIR-wf1-SRHGLE; Dmean-wf1-LRHGLE; Dmean-nonwf-median; T2-FLAIR-wf2-IMC2; T2-FLAIR-wf1-LRHGLE; T2-FLAIR-wf1-median; Dmean-wf1-skewness; T2-FLAIR-wf1-HGLRE; MK-wf1-mad]	168.9
Grade III vs. IV	β = [0.0142; 0.2603; -14.65; 14.05; 9.473; -0.002363; 0.7001] X = [MK-wf4-energy; MK-wf1-mad; MK-wf2-rms; MK-wf2-std; MK-wf4-median; MK-wf1-var; MK-wf1-std]	-62.44
Low vs High Grade	β = [0.6669; 0.03001; -18.81; -0.6598; -1.728E-05; -0.0003503; -0.00389]; X = [Dmean-wf1-Autocorrelation; MK-nonwf-median; T2-FLAIR-wf4-IMC2; Dmean-wf1-Variance; MK-nonwf-energy; Dmean-wf1-LRHGLE; T2-FLAIR-wf1-SRHGLE]	8.895
Positive vs Highly positive Ki-67 LI	β = [-0.01476; 0.01075; 0.00642]; X = [Dmean-wf1-median; Dmean-wf1-rms; MK-nonwf-mean]	0.2698

Imbalanced-adjusted logistic regression combining feature selection by maximizing the area under the receiver operating characteristic curve $(AUC)_{632+}$ metric in 100 bootstrap training and testing samples was implemented in the multivariate analysis. The repeatability and robustness of this method have been proven by Zhou et al. [41], and a similar result was obtained in our previous research [42]. Although no training/testing datasets from other research centres were included in our study, the obtained models were validated within 1000× bootstrapping, which allowed us to estimate how the model would behave in a validation set. Moreover, the number of citations of this method, as proposed by Vallieres and colleagues [31], guarantees the robustness of this method. Considering the relatively acceptable scanning time of DKI and high predictive performances of MK radiomics models, the implementation of multi-parameter MRI radiomics models integrating DKI radiomics in the clinic might be worthy of consideration and recommendation.

Limitations

Several limitations in our research should be noted. First, although high accuacies in the diagnostic performances in predicting glioma pathological profiles were achieved, the potential selection bias of tissue sample acquisition in surgical operation might have led to inaccurate identification of glioma subtypes; a point-to-point analysis might be much more demonstrative. Second, considering the priority of DKI in detecting the microstructure of white matter in the brain and the fact that gliomas are derived from glial cells, a prospective study of DKI radiomics in predicting glioma subtypes will be more persuasive. Moreover, radiomics features can be more comprehensively reflect intra-tumoral heterogeneity, and the intra-tumoral heterogeneity is significantly correlated with the overall survival of glioma patients. Our results highlight the feasibility of exploring the potential correlations between T2-FLAIR, DWI and DKI radiomics and patient prognosis.

Conclusion

Our research demonstrates the feasibility of radiomics based on T2-FLAIR imaging, DWI and DKI in the precise prediction of glioma pathological features and highlights the closer correlations of MK radiomics with the tumour grade and Ki-67 LI. MK radiomics allows precise glioma stratification, especially for grade III and IV gliomas. The combination of T2-FLAIR imaging, DWI and DKI allows for an accurate identification of glioma subtypes; thus, an evaluation of tumour profiles with combined models integrating DKI radiomics is recommended for glioma management.

Acknowledgements

We thank Dr. Kun Zhao and Yong Liu from Brainnetome Center & National Institute of Automation, Chinese Academy of Sciences, Beijing, China, for their generous help with radiomics feature extraction. This work was supported by grants from the National Program of the Ministry of Science and Technology of China during the “12th Five-Year Plan” (ID: 2011BAI08B10) and the National Natural

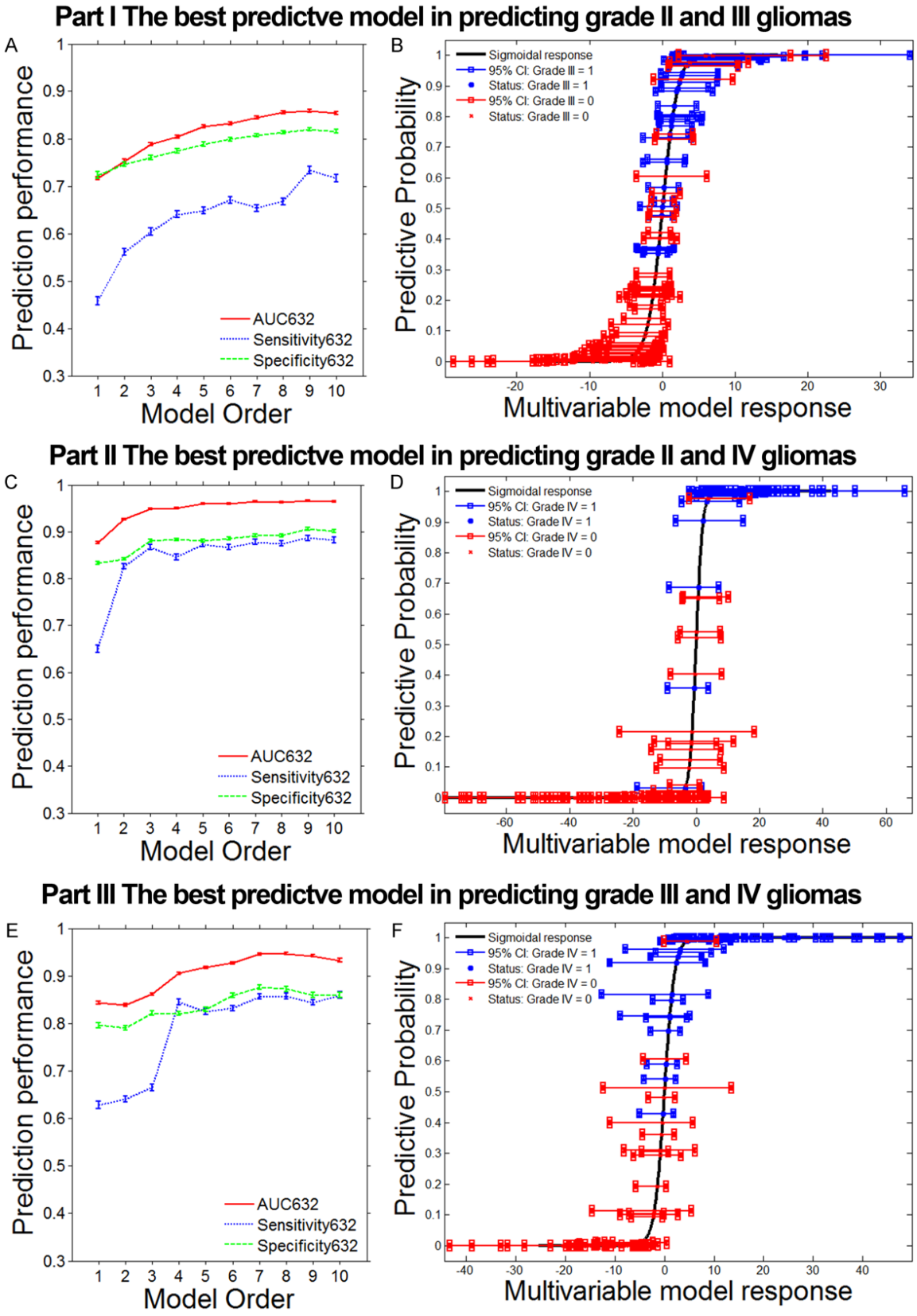

Figure 4. Models 1-10 and the best predictive models for differentiating grade II, III and IV gliomas. Diagnostic performances of the best predictive model in each subgroup analysis (A and B for grade II vs. III gliomas, C and D for

grade II vs. IV gliomas, and E and F for grade III vs. IV gliomas). The AUCs, sensitivities and specificities of models 1-10 in each subgroup analysis are displayed in A, C and E. The best predictive models were obtained when a combination of all maps was used (for grade II vs. III gliomas and grade II vs. IV gliomas) and MK radiomics (for grade III vs. IV gliomas). The corresponding predictive effect of each subgroup analysis is displayed on the right, in which high-grade gliomas are marked in blue, and low-grade gliomas are marked in red. The right side of the sigmoid maps exhibits excellent diagnostic performance with the best predictive models, and the left linear map displays the AUCs, sensitivities and specificities from models 1-10.

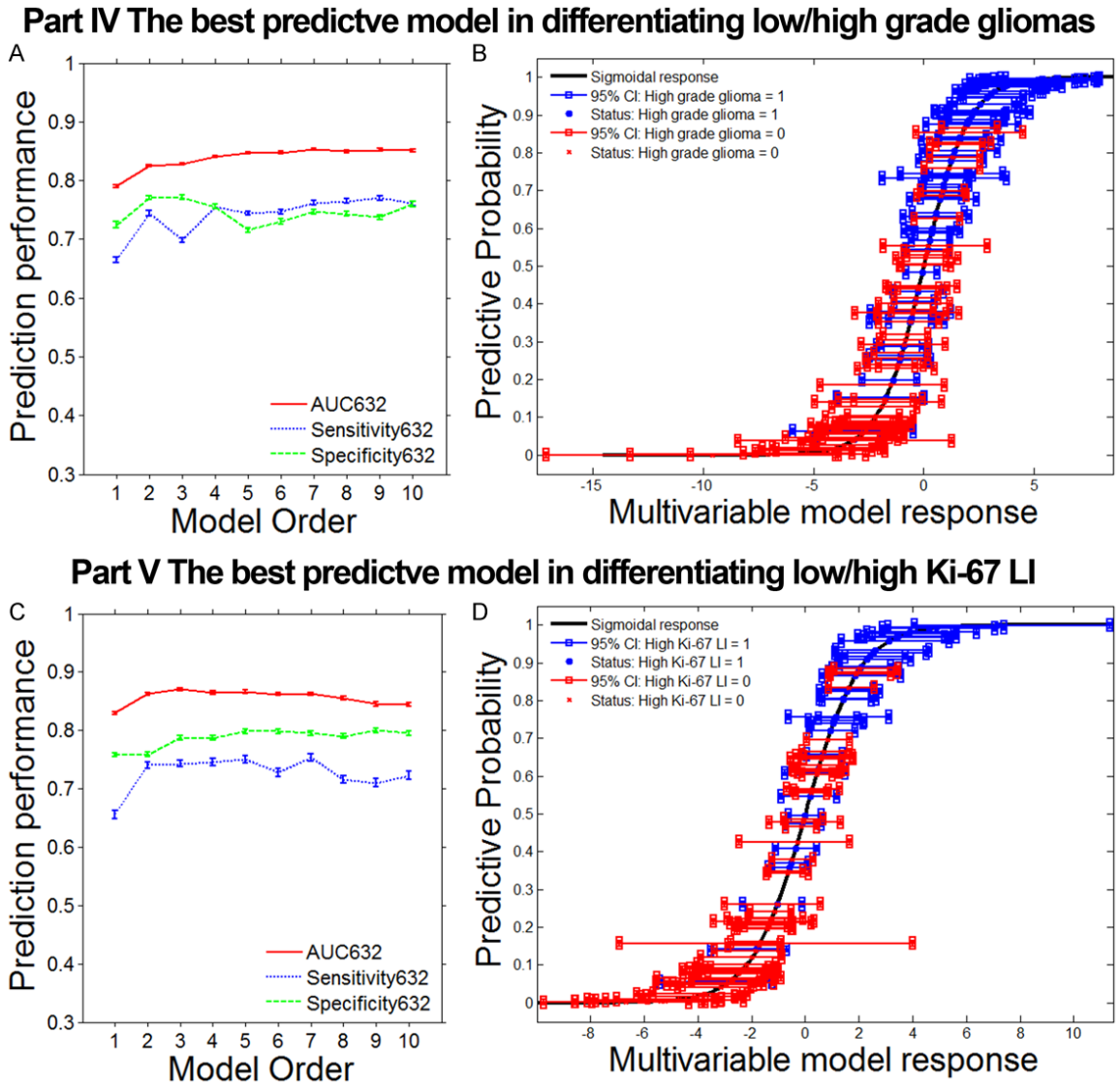

Figure 5. Models 1-10 and the best predictive models for differentiating low-/high-grade gliomas and the Ki-67 LI. The combination of all contrast maps resulted in the best predictive models for predicting low-/high-grade gliomas and the Ki-67 LI. A and C show the AUCs, sensitivities and specificities of models 1-10, while B and D display the predictive effect of the best predictive models in differentiating tumour types, in which high-grade gliomas and the higher Ki-67 LI are marked in blue and low-grade gliomas are marked in red.

Science Foundation of China (No. 81171308, No. 81570462, and No. 81730049).

Disclosure of conflict of interest

None.

Abbreviations

DWI, Diffusion-weighted imaging; DTI, Diffusion tensor imaging; DKI, Diffusion kurtosis imaging; LGG, Low-grade glioma; HGG, High-grade glioma; T2FSE, Transverse T2-weighted fast

spin echo; T1FLAIR, T1 fluid-attenuated inversion recovery; T2-FLAIR, T2 fluid-attenuated inversion recovery; T1C, T1 post-contrast enhancement; FA, Fractional anisotropy; ADC, Apparent diffusion coefficient; Dmean, Mean diffusion coefficient; MK, Mean kurtosis.

Address correspondence to: Shun Zhang, Department of Radiology, Tongji Hospital, Tongji Medical College, Huazhong University of Science and Technology, No. 1095, Jiefang Avenue, Wuhan 430030, Hubei, China. Tel: +86-13307178530; E-mail: zhangshun20050927@163.com

References

[1] Wen PY and Kesari S. Malignant gliomas in adults. N Engl J Med 2008; 359: 492-507.

[2] Stupp R, Mason WP, van den Bent MJ, Weller M, Fisher B, Taphoorn MJ, Belanger K, Brandes AA, Marosi C, Bogdahn U, Curschmann J, Janzer RC, Ludwin SK, Gorlia T, Allgeier A, Lacombe D, Cairncross JG, Eisenhauer E and Mirimanoff RO; European Organisation for Research and Treatment of Cancer Brain Tumor and Radiotherapy Groups and National Cancer Institute of Canada Clinical Trials Groups. Radiotherapy plus concomitant and adjuvant temozolomide for glioblastoma. N Engl J Med 2005; 352: 987-96.

[3] Yan H, Parsons DW, Jin G, McLendon R, Rasheed BA, Yuan W, Kos I, Batinic-Haberle I, Jones S, Riggins GJ, Friedman H, Friedman A, Reardon D, Herndon J, Kinzler KW, Velculescu VE, Vogelstein B and Bigner DD. IDH1 and IDH2 mutations in gliomas. N Engl J Med 2009; 360: 765-73.

[4] Ostrom QT, Bauchet L, Davis FG, Deltour I, Fisher JL, Langer CE, Pekmezci M, Schwartzbaum JA, Turner MC, Walsh KM, Wrensch MR and Barnholtz-Sloan JS. The epidemiology of glioma in adults: a "state of the science" review. Neuro Oncol 2014; 16: 896-913.

[5] Pignatti F, van den Bent M, Curran D, Debruyne C, Sylvester R, Therasse P, Afra D, Cornu P, Bolla M, Vecht C and Karim AB; European Organization for Research and Treatment of Cancer Brain Tumor Cooperative Group, European Organization for Research and Treatment of Cancer Radiotherapy Cooperative Group. Prognostic factors for survival in adult patients with cerebral low-grade glioma. J Clin Oncol 2002; 20: 2076-84.

[6] Wrensch M, Rice T, Miike R, McMillan A, Lamborn KR, Aldape K and Prados MD. Diagnostic, treatment, and demographic factors influencing survival in a population-based study of adult glioma patients in the San Francisco Bay Area. Neuro Oncol 2006; 8: 12-26.

[7] Mucha-Malecka A, Glinski B, Hetnal M, Jarosz M, Urbanski J, Fraczek-Blachut B, Dymek P, Malecki K and Chrostowska A. Long-term follow-up in adult patients with low-grade glioma (WHO II) postoperatively irradiated. Analysis of prognostic factors. Rep Pract Oncol Radiother 2012; 17: 141-5.

[8] Chen WJ, He DS, Tang RX, Ren FH and Chen G. Ki-67 is a valuable prognostic factor in gliomas: evidence from a systematic review and meta-analysis. Asian Pac J Cancer Prev 2015; 16: 411-20.

[9] Wang PF, Liu N, Song HW, Yao K, Jiang T, Li SW and Yan CX. IDH-1R132H mutation status in diffuse glioma patients: implications for classification. Oncotarget 2016; 7: 31393-400.

[10] Viallon M, Cuvinciuc V, Delattre B, Merlini L, Barnaure-Nachbar I, Toso-Patel S, Becker M, Lovblad KO and Haller S. State-of-the-art MRI techniques in neuroradiology: principles, pitfalls, and clinical applications. Neuroradiology 2015; 57: 441-67.

[11] Zonari P, Baraldi P and Crisi G. Multimodal MRI in the characterization of glial neoplasms: the combined role of single-voxel MR spectroscopy, diffusion imaging and echo-planar perfusion imaging. Neuroradiology 2007; 49: 795-803.

[12] Neumann-Haefelin T, Wittsack HJ, Wenserski F, Siebler M, Seitz RJ, Modder U and Freund HJ. Diffusion- and perfusion-weighted MRI. The DWI/PWI mismatch region in acute stroke. Stroke 1999; 30: 1591-7.

[13] Bello L, Gambini A, Castellano A, Carrabba G, Acerbi F, Fava E, Giussani C, Cadiolib M, Blasi V, Casarotti A, Papagno C, Gupta AK, Gaini S, Scotti G and Falini A. Motor and language DTI Fiber Tracking combined with intraoperative subcortical mapping for surgical removal of gliomas. Neuroimage 2008; 39: 369-82.

[14] Jensen JH, Helpern JA, Ramani A, Lu H and Kaczynski K. Diffusional kurtosis imaging: the quantification of non-gaussian water diffusion by means of magnetic resonance imaging. Magn Reson Med 2005; 53: 1432-40.

[15] Jiang R, Jiang J, Zhao L, Zhang J, Zhang S, Yao Y, Yang S, Shi J, Shen N, Su C, Zhang J and Zhu W. Diffusion kurtosis imaging can efficiently assess the glioma grade and cellular proliferation. Oncotarget 2015; 6: 42380-93.

[16] Falk Delgado A, Nilsson M, van Westen D and Falk Delgado A. Glioma grade discrimination with MR diffusion kurtosis imaging: a meta-analysis of diagnostic accuracy. Radiology 2018; 287: 119-127.

[17] Lambin P, Rios-Velazquez E, Leijenaar R, Carvalho S, van Stiphout RG, Granton P, Zegers CM, Gillies R, Boellard R, Dekker A and Aerts HJ. Radiomics: extracting more information from

medical images using advanced feature analysis. Eur J Cancer 2012; 48: 441-446.
[18] Gillies RJ, Kinahan PE and Hricak H. Radiomics: images are more than pictures, they are data. Radiology 2016; 278: 563-577.
[19] Parekh V and Jacobs MA. Radiomics: a new application from established techniques. Expert Rev Precis Med Drug Dev 2016; 1: 207-226.
[20] Kickingereder P, Neuberger U, Bonekamp D, Piechotta PL, Gotz M, Wick A, Sill M, Kratz A, Shinohara RT, Jones DTW, Radbruch A, Muschelli J, Unterberg A, Debus J, Schlemmer HP, Herold-Mende C, Pfister S, von Deimling A, Wick W, Capper D, Maier-Hein KH and Bendszus M. Radiomic subtyping improves disease stratification beyond key molecular, clinical, and standard imaging characteristics in patients with glioblastoma. Neuro Oncol 2018; 20: 848-857.
[21] Vallieres M, Kay-Rivest E, Perrin LJ, Liem X, Furstoss C, Aerts H, Khaouam N, Nguyen-Tan PF, Wang CS, Sultanem K, Seuntjens J and El Naqa I. Radiomics strategies for risk assessment of tumour failure in head-and-neck cancer. Sci Rep 2017; 7: 10117.
[22] Zhang B, He X, Ouyang F, Gu D, Dong Y, Zhang L, Mo X, Huang W, Tian J and Zhang S. Radiomic machine-learning classifiers for prognostic biomarkers of advanced nasopharyngeal carcinoma. Cancer Lett 2017; 403: 21-27.
[23] Xi YB, Guo F, Xu ZL, Li C, Wei W, Tian P, Liu TT, Liu L, Chen G, Ye J, Cheng G, Cui LB, Zhang HJ, Qin W and Yin H. Radiomics signature: a potential biomarker for the prediction of MGMT promoter methylation in glioblastoma. J Magn Reson Imaging 2018; 47: 1380-1387.
[24] Bae S, Choi YS, Ahn SS, Chang JH, Kang SG, Kim EH, Kim SH and Lee SK. Radiomic MRI phenotyping of glioblastoma: improving survival prediction. Radiology 2018; 289: 797-806.
[25] Lu CF, Hsu FT, Hsieh KL, Kao YJ, Cheng SJ, Hsu JB, Tsai PH, Chen RJ, Huang CC, Yen Y and Chen CY. Machine learning-based radiomics for molecular subtyping of gliomas. Clin Cancer Res 2018; 24: 4429-4436.
[26] Louis DN, Perry A, Reifenberger G, von Deimling A, Figarella-Branger D, Cavenee WK, Ohgaki H, Wiestler OD, Kleihues P and Ellison DW. The 2016 World Health Organization classification of tumors of the central nervous system: a summary. Acta Neuropathologica 2016; 131: 803-20.
[27] Aley N, Launchbury F, Richard-Loendt A, deBoer J, Chen S, Wang L, von Deimling A, Li N, Brandner S, Pouget C and Hergalant S. Ki-67 and MCM6 labeling indices are correlated with overall survival in anaplastic oligodendroglioma, IDH1-mutant and 1p/19q-codeleted: a multicenter study from the French POLA network. Brain Pathol 2020; 30: 465-478.
[28] Tabesh A, Jensen JH, Ardekani BA and Helpern JA. Estimation of tensors and tensor-derived measures in diffusional kurtosis imaging. Magn Reson Med 2011; 65: 823-36.
[29] Aerts HJ, Velazquez ER, Leijenaar RT, Parmar C, Grossmann P, Carvalho S, Bussink J, Monshouwer R, Haibe-Kains B, Rietveld D, Hoebers F, Rietbergen MM, Leemans CR, Dekker A, Quackenbush J, Gillies RJ and Lambin P. Decoding tumour phenotype by noninvasive imaging using a quantitative radiomics approach. Nat Commun 2014; 5: 4006.
[30] Benjamini Y and Hochberg Y. Controlling the false discovery rate: a practical and powerful approach to multiple testing. J R Stat Soc Series B Stat Methodol 1995; 57: 289-300.
[31] Vallieres M, Freeman CR, Skamene SR and El Naqa I. A radiomics model from joint FDG-PET and MRI texture features for the prediction of lung metastases in soft-tissue sarcomas of the extremities. Phys Med Biol 2015; 60: 5471-96.
[32] Sahiner B, Chan HP and Hadjiiski L. Classifier performance estimation under the constraint of a finite sample size: resampling schemes applied to neural network classifiers. Neural Netw 2008; 21: 476-83.
[33] McGranahan N and Swanton C. Biological and therapeutic impact of intratumor heterogeneity in cancer evolution. Cancer Cell 2015; 27: 15-26.
[34] Leng Y, Wang X, Liao W and Cao Y. Radiomics in gliomas: a promising assistance for glioma clinical research. Zhong Nan Da Xue Xue Bao Yi Xue Ban 2018; 43: 354-359.
[35] Kumar V, Gu Y, Basu S, Berglund A, Eschrich SA, Schabath MB, Forster K, Aerts HJ, Dekker A, Fenstermacher D, Goldgof DB, Hall LO, Lambin P, Balagurunathan Y, Gatenby RA and Gillies RJ. Radiomics: the process and the challenges. Magn Reson Imaging 2012; 30: 1234-48.
[36] Reith W, Hasegawa Y, Latour LL, Dardzinski BJ, Sotak CH and Fisher M. Multislice diffusion mapping for 3-D evolution of cerebral ischemia in a rat stroke model. Neurology 1995; 45: 172-7.
[37] Lyng H, Haraldseth O and Rofstad EK. Measurement of cell density and necrotic fraction in human melanoma xenografts by diffusion weighted magnetic resonance imaging. Magn Reson Med 2000; 43: 828-36.
[38] Inoue T, Ogasawara K, Beppu T, Ogawa A and Kabasawa H. Diffusion tensor imaging for preoperative evaluation of tumor grade in gliomas. Clin Neurol Neurosurg 2005; 107: 174-80.

[39] Jensen JH and Helpern JA. MRI quantification of non-Gaussian water diffusion by kurtosis analysis. NMR Biomed 2010; 23: 698-710.
[40] Takahashi S, Takahashi W, Tanaka S, Haga A, Nakamoto T, Suzuki Y, Mukasa A, Takayanagi S, Kitagawa Y, Hana T, Nejo T, Nomura M, Nakagawa K and Saito N. Radiomics analysis for glioma malignancy evaluation using diffusion kurtosis and tensor imaging. Int J Radiat Oncol Biol Phys 2019; 105: 784-791.
[41] Zhou H, Vallieres M, Bai HX, Su C, Tang H, Oldridge D, Zhang Z, Xiao B, Liao W, Tao Y, Zhou J, Zhang P and Yang L. MRI features predict survival and molecular markers in diffuse lower-grade gliomas. Neuro Oncol 2017; 19: 862-870.
[42] Su C, Jiang J, Zhang S, Shi J, Xu K, Shen N, Zhang J, Li L, Zhao L, Zhang J, Qin Y, Liu Y and Zhu W. Radiomics based on multicontrast MRI can precisely differentiate among glioma subtypes and predict tumour-proliferative behaviour. Eur Radiol 2019; 29: 1986-1996.

Supplementary Abbreviations for Figure 2 and Table 4

The abbreviations for names of radiomics features were listed as below: energy, kurtosis, maximum, mean, mad, median, minimum, range, rms, skewness, std, entropy, uniformity, var, Autocorrelation, Cluster Prominence, Cluster Shade, Cluster Tendency, Contrast, Correlation, Difference Entropy, Dissimilarity, Energy, Entropy, Homogeneity1, Homogeneity2, IMC1, IMC2, IDMN, IDN, Inverse Variance, Maximum Probability, Sum Average, Sum Entropy, Sum Variance, Variance, Short Run Emphasis, Long Run Emphasis, GLNU, RLNU, Run Percentage, LGLRE, HGLRE, SRLGLE, SRHGLE, LRLGLE, LRHGLE. The full name and detailed definition for each radiomics feature can be found in the supplementary materials listed in the following legends.

Definition of the used radiomics features

The present study used the same radiomics features as the previous study (Aerts et al., 2014). For readability, we have attached definitions of each feature below.

Briefly, radiomics features were divided into (i) first-order statistics; (ii) shape- and size-based features; (iii) textural features; and (iv) wavelet features.

(i) First-order statistics

Feature names	Definition
Energy	$\sum_{i}^{N} X(i)^2$
Entropy	$\sum_{i=1}^{N_t} P(i) log_2 P(i)$
Kurtosis	$\frac{\frac{1}{N}\sum_{i=1}^{N}(X(i)-\bar{X})^4}{(\sqrt{\frac{1}{N}\sum_{i=1}^{N}(X(i)-\bar{X})^2})^2}$
Maximum	The maximum intensity value of X
Mean	$\frac{1}{N}\sum_{i}^{N} X(i)$
Mean absolute deviation	The mean of the absolute deviations of all voxel intensities around the mean intensity value.
Median	The median intensity value of X
Minimum	The minimum intensity value of X
Range	The range of intensity values of X
Root mean square (RMS)	$\sqrt{\frac{\sum_{i}^{N} X(i)^2}{N}}$
Skewness	$\frac{\frac{1}{N}\sum_{i=1}^{N}(X(i)-\bar{X})^3}{\left(\sqrt{\frac{1}{N}\sum_{i=1}^{N}(X(i)-\bar{X})^2}\right)^3}$
Standard deviation	$\left(\frac{1}{N-1}\sum_{i=1}^{N}(X(i)-\bar{X})^2\right)^{1/2}$
Uniformity	$\sum_{i=1}^{N_l} P(i)^2$
Variance	$\frac{1}{N-1}\sum_{i=1}^{N}(X(i)-\bar{X})^2$

Note: $\bar{x}$ is the mean of χ. First-order statistics describe the distribution of voxel intensities within volume of interests (VOIs) in each contrast image.

(ii) Shape and size based features

Names	Definition
Compactness 1	$\frac{V}{\sqrt{\pi}A^{\frac{2}{3}}}$
Compactness 2	$36\pi\frac{V^2}{A^3}$
Maximum 3D diameter	The largest pairwise Euclidean distance, between voxels on the surface of the tumour volume
Spherical disproportion	$\frac{A}{4\pi R^2}$
Sphericity	$\frac{\pi^{\frac{1}{3}}(6V)^{\frac{2}{3}}}{A}$
Surface area	$\sum_{i=1}^{N}\frac{1}{2}\left\|a_i b_i \times a_i c_i\right\|$
Surface to volume ratio	$\frac{A}{V}$
Volume	The volume (V) of the tumour is determined by counting the number of pixels in the tumour region and multiplying this value by the voxel size

Note: *V* denotes the volume, and *A* denotes the surface area of the VOI. The surface area is calculated by triangulation (i.e., dividing the surface into connected triangles), where N is the total number of triangles covering the surface and a, b and c are edge vectors of the triangles. Shape- and size-based features describe the three-dimensional size and shape of VOI.

(iii) Textural features

Textural features, calculated from gray level co-occurrence (GLCM) (Haralick et al., 1973) and gray level run-length (GLRLM) (Galloway, 1975) texture matrices, describe patterns or the spatial distribution of voxel intensities in VOIs.

(a) Grey level co-occurrence matrix-based features

A GLCM is defined as P (i, j; δ, α), a matrix with size $N_g \times N_g$ describing the second-order joint probability function of an image, where the (i, j)th element represents the number of times the combination of intensity levels i and j occurs in two pixels in the image, which are separated by a distance of δ pixels in direction α, and N_g is the number of discrete gray level intensities.

Distance δ was set to 1, and direction α was set to each of the 13 directions in three dimensions, yielding a total of 13 gray-level co-occurrence matrices for each 3D image. From these gray level co-occurrence matrices, several textural features are derived. Each 3D gray level co-occurrence-based feature was then calculated as the mean of the feature calculations for each of the 13 directions.

Let:

P(i, j) is the co-occurrence matrix for an arbitrary δ and α

N_g is the number of discrete intensity levels in the image

μ is the mean of P(i, j)

$P_x(i) = \sum_{j=1}^{N_g} P(i, j)$ is the marginal row probabilities

$P_y(i) = \sum_{i=1}^{N_g} P(i, j)$ is the marginal column probabilities

u_x is the mean of p_x,

u_y is the mean of p_y,

δ_x is the standard deviation of p_x,

δ_y is the standard deviation of p_y,

$p_{x+y}(k) = \sum_{i=1}^{N_g} \sum_{j=1}^{N_g} P(i, j)$, $i+j = k$, $k = 2, 3, ..., 2N_g$,

$p_{x-y}(k) = \sum_{i=1}^{N_g} \sum_{j=1}^{N_g} P(i, j)$, $|i-j| = k$, $k = 0, 1, ..., N_g-1$,

$HX = -\sum_{i=1}^{N_g} p_x(i) \log_2 [p_x(i)]$ is the entropy of p_x,

$HY = -\sum_{i=1}^{N_g} p_y(i) \log_2 [p_y(i)]$ is the entropy of p_y,

$H = -\sum_{i=1}^{N_g} \sum_{j=1}^{N_g} P(i, j) \log_2 [P(i, j)]$ is the entropy of P(i, j),

$HXY1 = -\sum_{i=1}^{N_g} \sum_{j=1}^{N_g} P(i, j) \log(p_x(i)p_y(i))$,

$HXY2 = -\sum_{i=1}^{N_g} \sum_{j=1}^{N_g} p_x(i)p_y(i) \log(p_x(i)p_y(i))$,

Name	Definition
Autocorrelation	$\sum_{i=1}^{N_g} \sum_{j=1}^{N_g} ij\, P(i, j)$
Cluster prominence	$\sum_{i=1}^{N_g} \sum_{j=1}^{N_g} [i+j-\mu_x(i)-\mu_y(j)]^4 P(i, j)$
Cluster shade	$\sum_{i=1}^{N_g} \sum_{j=1}^{N_g} [i+j-\mu_x(i)-\mu_y(j)]^3 P(i, j)$
Cluster tendency	$\sum_{i=1}^{N_g} \sum_{j=1}^{N_g} [i+j-\mu_x(i)-\mu_y(j)]^2 P(i, j)$
Contrast	$\sum_{i=1}^{N_g} \sum_{j=1}^{N_g} \lvert i-j \rvert^2 P(i, j)$
Correlation	$\frac{\sum_{i=1}^{N_g} \sum_{j=1}^{N_g} ij\, P(i,j) - \mu_i(i)\mu_j(j)}{\sigma_x(i)\sigma_y(j)}$
Difference entropy	$\sum_{i=0}^{N_g-1} P_{x-y}(i) \log_2 [P_{x-y}(i)]$
Dissimilarity	$\sum_{i=1}^{N_g} \sum_{j=1}^{N_g} \lvert i-j \rvert P(i, j)$
Energy	$\sum_{i=1}^{N_g} \sum_{j=1}^{N_g} P(i, j)^2$
Entropy (H)	$\sum_{i=1}^{N_g} \sum_{j=1}^{N_g} P(i, j) \log_2 P(i, j)$
Homogeneity 1	$\sum_{i=1}^{N_g} \sum_{j=1}^{N_g} \frac{P(i, j)}{1 + \lvert i - j \rvert}$
Homogeneity 2	$\sum_{i=1}^{N_g} \sum_{j=1}^{N_g} \frac{P(i, j)}{1 + \lvert i - j \rvert^2}$
Informational measure of correlation 1 (IMC1)	$\frac{HXY - HXY1}{max\{HX, HY\}}$

Informational measure of correlation 2 (IMC2)	$\sqrt{1 - e^{-2(HXY2 - HXY)}}$
Inverse difference moment normalized (IDMN)	$\sum_{i=1}^{Ng}\sum_{j=1}^{Ng}\frac{P(i,j)}{1+(\frac{\lvert i-j\rvert^2}{N^2})}$
Inverse difference normalized (IDN)	$\sum_{i=1}^{Ng}\sum_{j=1}^{Ng}\frac{P(i,j)}{1+(\frac{\lvert i-j\rvert}{N})}$
Inverse variance	$\sum_{i=1}^{Ng}\sum_{j=1}^{Ng}\frac{P(i,j)}{\lvert i-j\rvert^2}, i\neq j$
Maximum probability	$\max\{P(i,j)\}$
Sum average	$-\sum_{i=2}^{2Ng}[iP_{x+y}(i)]$
Sum entropy	$-\sum_{i=2}^{2Ng}P_{x+y}(i)\log_2[P_{x+y}(i)]$
Sum variance	$\sum_{i=2}^{2Ng}(i-SE)^2P_{x+y}(i)$
Variance	$\sum_{i=1}^{Ng}\sum_{j=1}^{Ng}(i-\mu)^2P(i,j)$

(b) Gray level run-length matrix-based features

Run length metrics quantify gray level runs in an image. A gray level run is defined as the length in number of pixels of consecutive pixels that have the same gray level value. In a gray level run length matrix p(i, j|θ), the (i, j)th element describes the number of times j a gray level i appears consecutively in the direction specified by θ, and N_g is the number of discrete gray level intensities.

The GLRL matrix was computed for every of the 13 directions in three dimensions, from which the textural features below were derived. Each 3D GLRL feature was then calculated as the mean of the feature values for each of the 13 directions.

Let:

p(i, j|θ) is the (I, j) th entry in the given run-length matrix p for a direction θ,

N_g the number of discrete intensity values in the image,

N_r the number of different run lengths,

N_p the number of voxels in the image.

Name	Definition
Short Run Emphasis (SRE)	$\frac{\sum_{i=1}^{Ng}\sum_{j=1}^{Nr}[\frac{p(i,j\mid\theta)}{j^2}]}{\sum_{i=1}^{Ng}\sum_{j=1}^{Nr}p(i,j\mid\theta)}$
Long Run Emphasis (LRE)	$\frac{\sum_{i=1}^{Ng}\sum_{j=1}^{Nr}j^2p(i,j\mid\theta)}{\sum_{i=1}^{Ng}\sum_{j=1}^{Nr}p(i,j\mid\theta)}$
Gray Level Non-Uniformity (GLN)	$\frac{\sum_{i=1}^{Ng}[\sum_{j=1}^{Nr}p(i,j\mid\theta)]^2}{\sum_{i=1}^{Ng}\sum_{j=1}^{Nr}p(i,j\mid\theta)}$
Run Length Non-Uniformity (RLN)	$\frac{\sum_{j=1}^{Nr}[\sum_{i=1}^{Ng}p(i,j\mid\theta)]^2}{\sum_{i=1}^{Ng}\sum_{j=1}^{Nr}p(i,j\mid\theta)}$

Run Percentage (RP)	$\sum_{i=1}^{Ng}\sum_{j=1}^{Nr}\frac{P(i,j\mid\theta)}{Np}$
Low Gray Level Run Emphasis (LGLRE)	$\frac{\sum_{i=1}^{Ng}\sum_{j=1}^{Nr}[\frac{p(i,j\mid\theta)}{i^2}]}{\sum_{i=1}^{Ng}\sum_{j=1}^{Nr}p(i,j\mid\theta)}$
High Gray Level Run Emphasis (HGLRE)	$\frac{\sum_{i=1}^{Ng}\sum_{j=1}^{Nr}i^2\,p(i,j\mid\theta)}{\sum_{i=1}^{Ng}\sum_{j=1}^{Nr}p(i,j\mid\theta)}$
Short Run Low Gray Level Emphasis (SRLGLE)	$\frac{\sum_{i=1}^{Ng}\sum_{j=1}^{Nr}[\frac{p(i,j\mid\theta)}{i^2j^2}]}{\sum_{i=1}^{Ng}\sum_{j=1}^{Nr}p(i,j\mid\theta)}$
Short Run High Gray Level Emphasis (SRHGLE)	$\frac{\sum_{i=1}^{Ng}\sum_{j=1}^{Nr}[\frac{p(i,j\mid\theta)i^2}{j^2}]}{\sum_{i=1}^{Ng}\sum_{j=1}^{Nr}p(i,j\mid\theta)}$
Long Run Low Gray Level Emphasis (LRLGLE)	$\frac{\sum_{i=1}^{Ng}\sum_{j=1}^{Nr}[\frac{p(i,j\mid\theta)j^2}{i^2}]}{\sum_{i=1}^{Ng}\sum_{j=1}^{Nr}p(i,j\mid\theta)}$
Long Run High Gray Level Emphasis (LRHGLE)	$\frac{\sum_{i=1}^{Ng}\sum_{j=1}^{Nr}p(i,j\mid\theta)i^2j^2}{\sum_{i=1}^{Ng}\sum_{j=1}^{Nr}p(i,j\mid\theta)}$

(iv) Wavelet features

The wavelet transform decouples textural information by decomposing the original image at low and high frequencies. In our study, a “near symmetric” wavelet (sym4) was applied to the original MR images with a similar schematic, as described in a previous study (Aerts et al., 2014). Briefly, a discrete, one-level and undecimated three-dimensional wavelet transform was applied to the VOI of each MR contrast image, which decomposes the original image into 8 decompositions.

Let L and H represent a low-pass and a high-pass (i.e., a wavelet) function, and the wavelet decompositions of images (X) can be labelled as X_{LLL}, X_{LLH}, X_{LHL}, X_{LHH}, X_{HLL}, X_{HLH}, X_{HHL} and X_{HHH}. For example, X_{LLL} is then interpreted as the high-pass sub band, resulting from directional filtering with a low-pass filter along the x-direction, a low-pas filter along the y-direction and a high-pass filter along the z-direction and is constructed as:

$$X_{LLL}(i,j,k) = \sum_{p=1}^{N_L}\sum_{q=1}^{N_L}\sum_{r=1}^{N_H} L(p)\,L(q)\,H(r)\,X(i+p, j+q, k+r)$$

where N_L is the length of filter L and N_H is the length of filter H. The other decompositions are constructed in a similar manner, applying their respective ordering of low- or high-pass filtering in the x-, y- and z-directions. Since the applied wavelet decomposition is undecimated, the size of each decomposition is equal to the original image, and each decomposition is shift invariant. Because of these properties, the original tumour delineation of the gross tumour volume can be applied directly to the decompositions after wavelet transform. For each decomposition, we computed the first-order statistics and the textural features as described above.

Supplementary References

[1] Aerts HJ, Velazquez ER, Leijenaar RT, Parmar C, Grossmann P, Carvalho S, Bussink J, Monshouwer R, Haibe-Kains B, Rietveld D, Hoebers F, Rietbergen MM, Leemans CR, Dekker A, Quackenbush J, Gillies RJ and Lambin

P. Decoding tumour phenotype by noninvasive imaging using a quantitative radiomics approach. Nat Commun 2014; 5: 4006.

[2] Gallowy MM. Texture analysis using gray level run lengths. Computer Graphics & Image Processing 1975; 4: 172-179.

[3] Haralck RM, Shanmuam K and Dinstein IH. Textural features for image classification. Systems Man & Cybernetics IEEE Transactions on smc-3. 193; 610-621.

Table S1. The demographic characteristics of the included gliomas

	Grade II gliomas (n = 67)	Grade III gliomas (n = 36)	Grade IV gliomas (n = 34)	Statistical parameters	*P* Value
Age	39.01±14.10	43.97±14.07	49.59±13.56	F = 4.66	0.004
Sex					
Male	38	19	22	χ^2 = 1.06	0.589
Female	29	17	12		
Ki-67 LI	3.97±4.55	14.78±12.47	37.62±22.56	F = 55.36	<0.0001

Note: Two grade I gliomas were not listed above. The differences in age and Ki-67 index were evaluated with one-way ANOVA, post hoc analysis was performed with the least significant difference method, and the differences in sex compositions in different grade gliomas were analysed with Fisher exact test.

Table S2. The scanning parameters of T2FLAIR, DWI and DKI

SeqName	FOV (mm^2)	ST (mm)	SG (mm)	Matrix	Slices	B-value	TE (ms)	TR (ms)
DKI	256	3.0	0.0	128×128	43	0, 1,250 and 2,500	76.1	6,500
DWI	240	5.0	1.5	160×160	20	1,000	65.5	3,000
T2-FLAIR	240	5.0	1.5	512×512	20	NA	106.6	8,000
T1C	240	5.0	1.5	512×512	20	NA	26.3	2,009.3
T2FSE	240	5.0	1.5	512×512	20	NA	106.4	4,644
T1	240	5.0	1.5	512×512	20	NA	23.4	2,992.3

Abbreviations: SeqName = Sequence name; FOV = Field of view; ST = Slice thickness; SG = Slice gap; Matrix represents acquisition matrix; TE = Echo time; TR = Repetition time; NA = Not applicable.

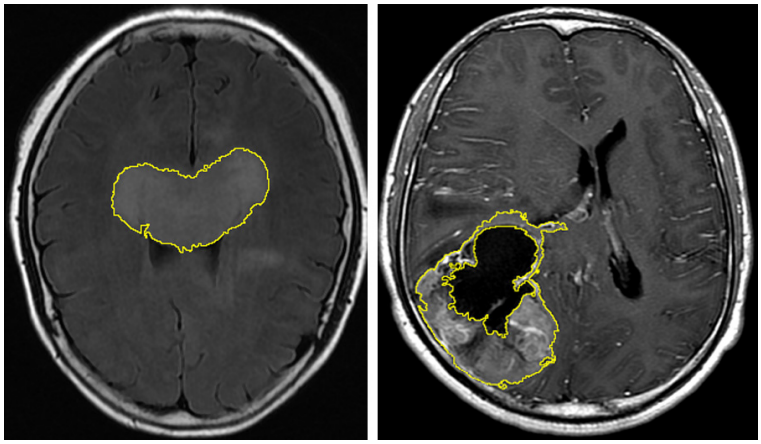

Figure S1. Representative cases for the definition of volume of interest in anatomical images. Note: Two representative cases of low-grade gliomas and high-grade gliomas are displayed above to clarify the definition of volume of interest (VOI). With the help of a semi-automatic method based on the threshold of MRI signal intensities, three-dimensional VOIs were segmented first according to signal intensities mainly on T2FLAIR and contrast-enhanced T1-weighted images to depict the general location of the tumour. Then, the obtained tumour areas were adjusted by an experienced radiologist. Moreover, diffusion weighted images, i.e., b1000 map was used to avoid necrotic and cystic areas. The three-dimensional VOIs were carefully drawn on the tumour parenchyma with all anatomical images and diffusion images to reduce the interference of necrotic and cystic areas and haemorrhage.

Table S3. The diagnostic performance of different contrast maps in differentiating low-high grade gliomas and different Ki-67 indexes

SeqName	Low- vs. High-grade gliomas			Positive vs. Highly positive Ki-67		
	AUC	Sen	Spec	AUC	Sen	Spec
ADC	0.828±0.002	0.791±0.004	0.75±0.004	0.843±0.004	0.739±0.006	0.788±0.004
Dmean	0.836±0.002	0.804±0.004	0.733±0.004	0.865±0.003	0.747±0.006	0.759±0.004
FA	0.706±0.003	0.63±0.005	0.66±0.005	0.75±0.005	0.61±0.008	0.736±0.005
T2FLAIR	0.797±0.003	0.703±0.005	0.736±0.005	0.811±0.003	0.723±0.007	0.766±0.004
MK	0.797±0.002	0.738±0.005	0.67±0.004	0.855±0.003	0.736±0.007	0.802±0.004
Total	0.853±0.002	0.762±0.004	0.747±0.004	0.87±0.003	0.743±0.006	0.788±0.004

Note: SeqName represents the name of each contrast map. AUC represents the area under curve. Sen represents sensitivity and Spec represents specificity for each sub-analysis.

Table S4. The diagnostic performances of different contrast maps in differentiating sub-grade gliomas

SeqName	Grade II vs. III			Grade II vs. IV			Grade III vs. IV		
	AUC	Sen	Spec	AUC	Sen	Spec	AUC	Sen	Spec
ADC	0.745±0.005	0.56±0.008	0.699±0.005	0.911±0.003	0.804±0.007	0.842±0.003	0.845±0.004	0.741±0.006	0.764±0.006
Dmean	0.777±0.005	0.68±0.007	0.721±0.005	0.947±0.002	0.875±0.00	0.874±0.004	0.828±0.004	0.744±0.006	0.764±0.006
FA	0.791±0.004	0.71±0.008	0.74±0.004	0.882±0.004	0.745±0.007	0.839±0.004	0.829±0.004	0.731±0.007	0.768±0.006
T2FLAIR	0.724±0.004	0.63±0.007	0.7±0.004	0.932±0.002	0.829±0.006	0.87±0.003	0.83±0.004	0.743±0.006	0.738±0.006
MK	0.715±0.004	0.46±0.008	0.725±0.007	0.916±0.002	0.803±0.006	0.862±0.004	0.947±0.003	0.857±0.006	0.872±0.005
Total	0.858±0.003	0.73±0.008	0.819±0.004	0.966±0.002	0.887±0.006	0.906±0.003	0.877±0.003	0.816±0.006	0.803±0.005

Note: SeqName represents the name of each contrast map. AUC represents the area under curve. Sen represents sensitivity and Spec represents specificity for each sub-analysis.